Journal of Materials Chemistry A

Accepted Manuscript

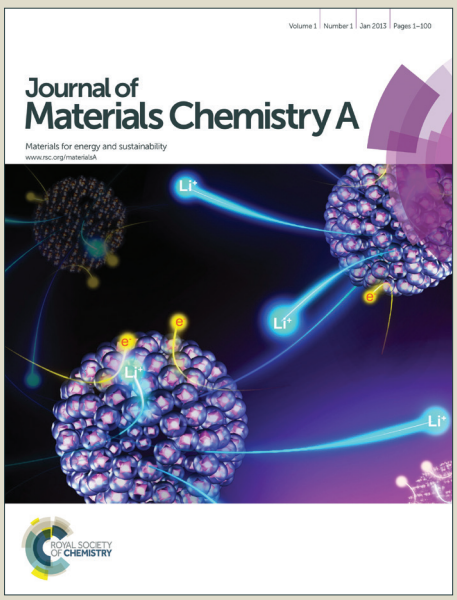

ROYAL SOCIETY OF CHEMISTRY

www.rsc.org/materialsA

Controllable Oxygenic Functional Groups of Metal-free Cathodes for High Performance Lithium Ion Batteries

Dongbin Xiong[a], Xifei Li[a,b]*, Hui Shan[a], Litian Dong[a], Ye Cao[a], Dejun Li[a]*

[a]Energy & Materials Engineering Centre, College of Physics and Materials Science, Tianjin Normal University, Tianjin 300387, China. E-mail: xfli2011@hotmail.com; dejunli@mail.tjnu.edu.cn

[b]Key Laboratory of Advanced Energy Materials Chemistry (Ministry of Education), C ollaborative Innovation Center of Chemical Science and Engineering, College of Che mistry, Nankai University, Tianjin 300071, China

Abstract

Poriferous reduced graphene oxide (rGO) with abundant oxygen-containing functional groups synthesized by one-step hydrothermal method was successfully employed as a high performance cathode in lithium-ion batteries. The electrochemical results show that rGO exhibit remarkable lithium storage capacity (up to 270 mAh g^{-1} after 100 cycles). The further analysis shows that the rGO can exhibit significantly high rate capacity, good reversibility, and excellent cycling stability, which clearly revealing the potential uses of the rGO as the cathode material to boost both energy and power densities of LIBs. Furthermore, by controlling oxygenic functional groups of rGO, it was demonstrated that the capacity increased with the increase of the

amount of oxygenic functional groups, which illustrates that their excellent electrochemical performance could be attributed to their specific poriferous structure and the oxygen-containing functional groups of rGO.

1. Introduction

Energy conversion/storage technology plays an important function in the development of modern society. The development of large-scale and low-volume energy-storage systems has been vitally important to satisfy the fast-growing demand for light-weight and high-capacity electrical storage, such as in electric vehicles and microelectro-mechanical devices[1, 2]. Among various energy-storage devices[3-5], lithium-ion batteries (LIBs) have became one of the best choices due to high working voltages, high energy density, flexible and lightweight design, long cycle life and environmental friendliness[2, 6]. Currently, in one LIB system, the commercial anode (say graphite) shows much higher specific capacity than the commercial cathode. Thus, how to increase the cathode energy capacity has been a significant challenge. The common active inorganic materials ($LiCoO_2$, $LiNiO_2$, Li_2MnO_4, $LiFePO_4$ etc[6-10]) as cathodes exist many limitations such as a low practical capacity (~160 mAh g^{-1}), unreliable safety, and the high cost of cobalt (Co) as well as environmental problem, which limit the further improvement and development of battery performance. Recently, three-component layered $LiNi_xCo_yMn_zO_2$ (NCM, $0 \leq x, y, z < 1$) has exhibited promising electrochemical properties as cathode materials[11, 12], but some

problems such as dissolution of transition metals occur at the electrode-electrolyte interface after long-term cycling, resulting in uncontrolled voltage changes and limited cycling stability[13, 14]. As a result, the research on lithium-ion batteries has been directed mainly towards the design of high capacity, good cycling stability and low cost cathode materials, which emerges a surging demand to develop environmentally friendly green cathode materials to replace the current several non-renewable and not environment-friendly cathodes. More importantly, the metal-free cathodes can reduce the cost of LIBs (partly due to the use of costly transition metals such as Co and Ni).

During the development of electrode materials in LIBs, 2D graphene nanosheets (GNSs) have played an important role and shown great promise to improve the LIB performance due to its advantages such as high electronic conductivity, good mechanical and chemical stability, unique material structures, high specific surface areas and broad electrochemical window, etc[15-17]. As a result, GNSs and its composites have been widely explored for LIB applications. For example, GNSs anodes show much higher reversible capacity than the commercial graphite[18, 19], furthermore, various graphene-based composite materials such as SnO_2/graphene[20-23] as anode and $LiFePO_4$/graphene[8, 24, 25] as cathode presented enhanced battery performance. Recently, it was highlighted that carbon nanotubes (CNTs) with functionalization could work as cathode materials of LIBs with high gravimetric of 230 Wh kg^{-1} at 2.6 kW kg^{-1} [26]. On basis of this strategy, it inevitably happened that some studies were focused on exploring the graphene with surface oxygen-containing functional groups as LIB cathodes. Importantly, the researchers demonstrated that

oxygen-containing functional groups (such as >C=O and-COOH) onto GNSs act as the reaction centers with lithium ions, which could rapidly and reversibly capture lithium ions through surface adsorption and/or surface redox reaction[26, 27], which agrees with the organic cathode materials as previously reported[28, 29]. Thus, the functionalized GNSs deliver exceptionally higher energy density (over 200 mAh g^{-1}) with long-lasting cyclability as well as high power density in comparison with the current active inorganic cathode materials[9, 30] (e.g., $LiCoO_2$, $LiNiO_2$ or $LiFePO_4$) and three-component layered NCM. However, the functionalized GNSs reported by the researchers show some difficulties in controlling oxygen-containing functional groups. Unfortunately, few research focus on the effects of amount of oxygen-containing functional groups on GNS cathode performance.

In this study, we report a simple strategy of hydrothermal approach to highly control the amount of oxygen-containing functional groups on GNSs. It is worth noting that to adjust the time of hydrothermal reaction can easily control the reduction degree of graphene oxide as well as the amount of oxygen-containing functional groups on reduced graphene oxide (rGO). Using this proposed strategy, we investigated the significant effects of functional group amount and types on lithium storage of GNS cathode.

2. Experimental Section

2.1 Synthesis of Graphite oxide (GO)

Graphite oxide (GO) was initially fabricated by modified Hummers method, as previously reported by our group[10]. The natural graphite (1 g) and $NaNO_3$ (0.75 g) were uniformly mixed, then 34 mL of H_2SO_4 (98%) was added into the mixture and stirred for 2 h in an ice bath, meanwhile, $KMnO_4$ (4.5 g) was slowly added to the dispersion. After the mixture was stirred for 5 days at room temperature, 100 mL of H_2SO_4 (5%) was added to the mixture and stirred for another 2 h. Then 5 mL of H_2O_2 (35%) were slowly added to the solution until the gas bubbles were not produced. The resultant graphite oxide was then repeatedly washed with HNO_3 (10%) aqueous solution. The GO was then thoroughly centrifugated with deionized (DI) water to obtain GO suspension. The GO suspension was finally dried at room temperature for 24 h to obtain GO.

2.2 Synthesis of reduced graphene oxide (rGO)

The as-prepared GO was ground into fine powder. The resultant powder was dispersed in water (160 mL) by ultrasonic cell disruption for 20 min to make a GO aqueous dispersion (3 mg mL^{-1}). The obtained brown dispersion was then centifuged for 30 min at 10000 rpm to remove some aggregates. A 40 mL portion of the obtained homogeneous GO aqueous dispersion was sealed in a 50 mL teflonlined autoclave, and the reaction was maintained at 180 ^{o}C for 0.5 h, 1 h, 6 h and 12 h, respectively. Then the obtained graphene hydrogel was freeze-dried to obtain rGO. The resultant

materials labelled as rGO-0.5, rGO-1, rGO-6 and rGO-12 are related to the reaction time of 0.5, 1, 6, 12 h, respectively.

2.3 Characterization

X-ray diffraction (XRD) was carried out using a D8 Advance X-ray diffractometer (XRD, Bruker, Germany) with Cu/Ka radiation in the range from 5^{o} to 85^{o} to study the structures of the resultant materials of GO, GO-I, rGO-I, rGO-II and rGO-III. The element composition of the sample was analyzed by energy dispersive X-ray spectroscopy (EDX, INCAx-sight, Oxford). X-ray photoelectron spectroscopy (XPS, VG ESCALAB MK II) was performed to determine the degree of oxidation and elemental composition of the obtained materials. The morphology of the samples was verified using field-emission scanning electron microscopy (FE-SEM, SU8010, Hitachi) and high-resolution transmission electron microscopy (HR-TEM, JEM-3000F). The functional groups on the materials were detected by Fourier transform infrared spectroscopy instrument (FTIR, IRAffinity-1, SHIMADZU) by using pressed KBr pellets. The Raman measurement of as-synthesized material was conducted on a confocal Micro Raman Spectrometer with LabRAM HR800 system (HORIBA, Korea) in the range of 1000-2000 cm^{-1}. The hydrophilic testing was performed to characterize the effects of oxygenic functional groups of the samples by Attension Theta SFE (ksv INSTRUMENTS).

2.4 Electrochemical Characterization

The working electrodes were fabricated by mixing the active material (reduced graphene oxide) with polyvinylidene fluoride binder (PVDF) and acetylene black with a weight ratio of 80:10:10 in an N-methyl-2-pyrrolidone (NMP) solvent to produce the slurry. The resulting slurry was uniformly pasted onto Al foil, dried in a vacuum oven at 90^{o}C for 12 h. The 2032 typed coin cells were assembled in a high purity argon-filled glove box using lithium metal as the anode and 1 M $LiPF_6$ (dissolved in a solvent consisting of 50% ethylene carbonate and 50% dimethyl carbonate by volume) as the electrolyte. The galvanostatic charge/discharge tests were performed using a Land battery testing system (LANHE CT2001A) in the voltage range of 1.5~4.5 V (vs. Li/Li^+). Cyclic voltammogram (CV) measurements were performed on Princeton Applied Research VersaSTAT 4 electrochemical workstation using a voltage range of 1.5~4.5 V (vs. Li/Li^+) at a scan rate of 0.1 mV s^{-1}. Electrochemical impedance spectroscopy (EIS) measurements were carried out on a Princeton Applied Research VersaSTAT 4 over a frequency range from 0.01 Hz to 100 kHz with the AC amplitude of 5.0 mV.

3. Results and Discussion

Scheme 1 shows the fabrication strategy of the reduced graphene oxide nanosheets (rGO) used as cathode materials. Firstly, graphite oxide was obtained by

modified Hummers' method, and then graphene oxide was exfoliated from graphite oxide through ultrasonic dispersion process. During this process the brown and well dispersed graphene oxide dispersion was obtained. The rGO hydrogel with different content of oxygen-containing functional group were then fabricated by adjusting the reaction time in the hydrothermal assembly process (see Experimental Section for details). During this process, graphene oxide was partial reduced, and some controlled functional groups were produced on rGO aerogel.

SEM and TEM images were performed to investigate the morphology and microstructure of the rGO materials. The SEM images of graphene oxide in Supporting Information Fig. S1 a and b reveal an ultrathin, wrinkled and curved gossamer-like structure originating from the thermodynamic stability of two-dimensional materials. The SEM images in Fig.1a, 1b and 1c show typical morphologies of the obtained rGO-1, rGO-6 and rGO-12 samples, respectively. The ultrathin and small layered platelets of graphene sheets can be clearly observed in high magnification SEM images. The obtained hydrothermally treated rGO exhibited porous character, and the nanosheet size of rGO-1, rGO-6 and rGO-12 greatly decreased compared with GO and rGO-0.5 nanosheets (see Fig S1 and Fig S2). However, obvious differences of rGO-1, rGO-6 and rGO-12 are found. The wrinkled graphene is composed of small layered platelets, as shown in Fig. 1 a. With the increase of hydrothermal treatment time, rGO shows a macro-porous morphology with the framework network, as can be seen in Fig.1 b and 1 c. It clearly indicates that the hydrothermal treatment time has a significant effect on rGO morphology.

TEM was used for further in-depth observation of the detail structures of rGO. Fig. 1d, e, f show that graphene layers from rGO exhibit a highly transparent gossamer sheets with some wrinkles visible, which agrees with the typical morphology as previously reported [31, 32]. The cross section image of rGO-1 (see Fig. S1 d) indicates that the synthesized rGO typically consisted only of a few layers, and the interlayer spacing is about 0.412nm, which is broad than natural graphite (interlayer spacing is 0.335nm) and narrow than GO (interlayer spacing is 0.6nm-1.2nm) that has been reported in the literature[33, 34]. Corresponding selected area electron diffraction (SAED) presents ring patterns without defined diffraction spots, as show inside the TEM images, suggesting that the obtained rGO was with multi-layer structure and structural irregularity due to the oxygen-containing functional group on the edge and plane of the multilayer rGO nanosheets [35, 36]. The abundant pores and loose spongy structure of the obtained rGO would effectively facilitate mass transport of the cathode [37, 38].

X-ray photoelectron spectroscopy (XPS) was employed for chemical analysis of surface functional groups on the rGO nanosheets. As shown in Fig. 2a, the survey spectra of all the samples (rGO-1, rGO-6 and rGO-12) show the presence of O 1s peak. This peak was attributed largely to the presence of oxygen containing functional groups on the rGO nanosheets [26]. The intensity of the O 1s peak becomes weaker from of rGO-1 to rGO-12, according with the results of quantitative elemental analysis in Fig. 2b. rGO-1 was with a residual of 18.37 at.% of O in comparison to 11.28 at.% of rGO-12, indicating that the oxygen containing functional groups of the

samples decrease with the extension of hydrothermal reaction time. Further analysis on the high resolution C 1s peaks revealed that the rGO samples contain carboxyl groups (COOR, 288.8 ± 0.1 eV in C 1s), hydroxyl and epoxy groups (C–O, 286. 5 ± 0.1 eV in C 1s), carbonyl groups (C=O, 288.1± 0.1 eV in C 1s) and C–C bonds (sp^2 carbon, 284.5 eV, sp^3 carbon, 285.2 eV), which is similar to the reported literatures[39-41]. Observed from the C 1s spectra in Fig. 2c, 2d and 2e, the oxygen functional groups of rGO-6 (O=C–OH, 1.5 at.%; >C=O, 7.8 at.%; >C–OH, 20.6 at.%) showed higher oxygen content compared to that of rGO-12 (O=C–OH, 3.12 at.%; >C=O, 9.81 at.%; >C–OH, 17.55 at.%) but with a less oxygen content compared to that of rGO-1 (O=C–OH, 2.3 at.%; >C=O, 4.3 at.%; >C–OH, 33.3 at.%), indicating that the longer hydrothermal treatment time of 12 h ensured the removal of more oxygen functional groups. The remaining functional groups of rGO samples could also be demonstrated by the O 1s spectra shown in Fig. 2f (rGO-1), 2g (rGO-6) and 2h (rGO-12), where the hydroxyl/epoxide (-OH, 532.5 ± 0.1 eV), carbonyl (C=O, 531.6 ± 0.1 eV) and carboxyl (O=C–OH, 533.4 ± 0.1 eV) groups[26] on the as-prepared rGO samples can be clearly identified, and the amount of each functional group is similar.

The local elemental composition of the as-prepared GO, rGO-0.5 and rGO samples is certified by EDX, and the results in Fig. 3a and Fig. S3 reveal that the GO sample contains the highest oxygen content, and the atomic ratio of O and C is about 0.538. The hydrothermal treatment results in the decrease of atomic ratio of O and C, and it reveals a trend that the oxygen-containing functional groups decrease with the

reaction time increase. More information on surface functional group of the rGO was studied by FT-IR spectroscopy (Fig. 3b). The characteristic absorption peaks of graphite oxide(GO), as expected, exhibits the presence of strong peaks corresponding to oxygen-containing groups at 1729cm^{-1} (C=O stretching vibration from carbonyl and carboxylic groups)[42], 1620cm^{-1} (aromatic C=C stretching vibration or absorbed water),1398cm^{-1} (O-H bending), 1227 and 872cm^{-1} (C-O-C of an epoxy group), and 1065cm^{-1} (C-O stretch of the alkoxy group)[40]. In addition, the broader peak around 3405 cm^{-1} is assigned to hydroxyl groups. These signals indicated that the rich oxygen-based functional groups were successfully grafted onto the GO surface and edge by modified Hummers method [33]. However, compared to GO, the intensities of rGO spectra associated with oxygen-containing groups decrease partly. Along with the reduction time increase, the H-O stretching vibration peaks at 3405 and 1398 cm^{-1} and the C-O stretching vibration peak at 1065 cm^{-1} dramatically decrease, even disappear. The C-O-C stretching vibration peak at 872cm^{-1} was directly disappeared. The FT-IR spectra of rGO-6 and rGO-12 are similar to that of rGO-1, but rGO-1 remains more hydroxyl groups and alkoxy groups according to the existence of H-O stretching vibration peaks at 3405 cm^{-1} and C-O stretching vibration peak at 1065 cm^{-1}. Thus, the comparison of FT-IR spectra indicates that GO is deoxidized and reduced through hydrothermal process, and the amount of oxygen-containing groups decline gradually as the reduction time increases.

Raman spectroscopy is one useful technique to characterize carbonaceous materials. The D band results from the structural disorder or defects present in

graphitic based materials; whereas the G band arises from sp2 bonded ordered graphitic carbon[43, 44]. As shown in Fig. 3c, two prominent peaks of GO appear at around 1355 and 1602 cm^{-1}, which are attributed to D and G band, respectively. The existence of D peak at 1355 cm^{-1} is a result of the oxidation-induced defects[45]. After reduction of hydrothermal process, the D and G peaks still exist, but the ratio of D to G band intensity (I_D/I_G) changes. I_D/I_G is commonly utilized to gauge the degree of structural disorder, and the higher values suggest more disorder along with smaller average graphitic crystalline size[46, 47]. The I_D/I_G values of the GO, rGO-1, rGO-6 and rGO-12 were 1.36, 1.80, 2.08 and 2.00, respectively, on the basis of the fitting of the Raman spectroscopy. The rGO shows higher I_D/I_G values compared to that of GO. The higher ratio indicates more disorder and defects, which was due to the introduction of defects such as bonding disorders and vacancies in the graphene lattice. The I_D/I_G values of rGO-6 (2.08) and rGO-12 (2.00) were higher than that of rGO-1 (1.80) mainly due to the formation of more bonding disorders and more vacancies in the graphene lattice.

Structural studies of GO, rGO-1, rGO-6 and rGO-12 were investigated by using X-ray diffraction method, as shown in Fig. 3d. As a reference, the XRD pattern of the natural graphite is shown in Fig. S4. The diffraction peak of the natural graphite appears at 26.6°, corresponding to an interlayer spacing of about 0.34 nm. Due to the insertion of oxygen-containing functional groups and H_2O molecules, the (002) diffraction peak of GO positions at 11.8°, with an enlarged interlayer spacing of 0.749 nm during the oxidation process[48]. The hydrothermal reduction of GO greatly

decreases the oxygenic groups and interlayer water[49]. As demonstrate in the XRD patterns, rGO-1 shows a broad (002) reflection peak at 24.8°, and the peaks of rGO-6 (26.9°) and rGO-12 (29.2°) gradually shift to higher diffraction angles, which is attributed to the decrease of interlayer distance due to the decreased surface functional groups[33]. In addition, the peak of a (100) reflection at around 41° is ascribed to the C–C in-plane length in the reticular system [50]. These observations confirm that the degree of reduction level of rGO samples was enlarged gradually with the increase of hydrothermal reaction time. This phenomenon suggests that most of the oxidized groups on the surface of GO had been removed after the hydrothermal process.

To further investigate oxygen-containing functional groups of the rGO samples, the hydrophilic test was performed by dripping distilled water on the surface of glass sheets which were coated with GO and various rGO samples, as shown in Fig. 4 a~d. It is obvious that the hydrophilic angles of GO, rGO-1, rGO-6 and rGO-12 are 64.62°, 76.1°, 83.58°, 87.13°, respectively. Since an increase of oxygen-containing functional groups enhances the hydrophilicity of the samples, it can be concluded that the content order of oxygen-containing functional groups of the samples is GO> rGO-1> rGO-6> rGO-12. This conclusion was in good agreement with the aforementioned analysis.

The electrochemical tests were performed via assembling coin cells using the as-prepared reduced graphene oxide nanosheets as cathodes. The CV measurements of the samples were conducted in the voltage range of 1.5 to 4.5 V with a scan rate of 0.1 mV s^{-1}, as shown in Fig. 5a. It can be seen that all of the rGO electrodes show a

reversible lithiation/delithiation process, which is similar to the previous reference[30, 51]. Differing from traditional transitional metal oxide cathode materials, no clear redox peak observed is due to its unique lithium storage (see Scheme 2). It can be observed that the rGO-1 sample shows much higher current responses than rGO-6 and rGO-12, and the integral area of CV curves of the rGO samples gradually decreased with the degree of reduction. Increasing of reduction time decreased the O/C ratio, thus, the CV results strongly suggest that the functional groups of rGO offer the electrochemical reaction center with lithium ions. Higher electrochemical activity of rGO-1 was attributed to an increase in lithium storage reactions of surface functional groups[30]. Moreover, there is no obvious profile difference in the first three cycles of CV curves of rGO-1 cathode electrode, as shown in Fig. S5a, indicating that the rGO-1 electrode shows high cyclicality.

The galvanostatic charge/discharge curves of the rGO-1 and GO cathode electrodes at various current densities with a voltage range from 1.5 to 4.5 V are shown in Figs. 5b and Figs. S5b, respectively, the potential increases (or decreases) smoothly as a function of the state of charge (or discharge), which is similar to the reported functionalized graphene cathode[37, 51]. The rGO-1 electrode shows a high reversible capacity of 257mAh g^{-1} at 50 mA g^{-1}. With an increase in the current densities, the rGO-1 cathode exhibited excellent average capacity as 221 mAh g^{-1} at 0.1A g^{-1}, 184 mAh g^{-1} at 0.2A g^{-1} and 169 mAh g^{-1} at 0.4A g^{-1}, respectively. The outstanding electrochemical properties of rGO cathodes are believed to be associated with the abundant oxygen functional groups on the surface, high electrical

conductivity and their fluffy porous structure which provide the efficient transport route for lithium ions in such rGO cathodes materials.

Fig. 5c presents the cycle performance of GO, rGO-1, rGO-6 and rGO-12 electrodes at 50 mA g^{-1} up to 100 cycles. The GO material exhibits poor cyclic performance with the specific capacity of 80 mA h g^{-1} after 100 cycles. By contrast, after GO reduction via hydrothermal method, the rGO electrodes show very stable cycle performance. The capacity increase of the rGO could be attributed to the activating process of the electrode, which was also observed in other research group[52]. Importantly, the rGO-1 electrode exhibits very high reversible capacity and stable cycle performance, producing a high and stable discharge capacity of about 280 mAh g^{-1} after 100 cycles. With the increase of reduction degree, the rGO-6 and rGO-12 electrodes exhibited decreased capacities of about 212 and 194 mAh g^{-1} after 100 cycles, respectively. Towards the decrease of reduction degree (say 0.5 h of hydrothermal reaction time), the cyclic performance of the resultant rGO-0.5 electrode is shown in Fig. S6a. Clearly, the rGO-0.5 reveals poorer performance with 113 mAh g^{-1} after 80 cycles. These results demonstrate that the oxygen-containing functional groups on the surface of rGO cathodes function as lithium storage sites. The GO surface possesses rich oxygen-containing functional groups, however, due to very low electrical conductivity, the GO and rGO-0.5 electrodes showed poorer cycling performance and lower specific capacity in comparison to the other rGO electrodes.

Fig. 5d presents the rate capability of GO, rGO-1, rGO-6, and rGO-12 at various

current densities (from 50 to 400 mA g^{-1}). Compared to the GO, rGO-6, and rGO-12 electrodes, the rGO-1 electrode displayed elevated capacity and superior stability at each current density. When the current density gradually increased from 50 to 100, 200 and 400 mA g^{-1}, the average discharge capacities of rGO-1 decreased from 257, to 221, 184 and 169 mAh g^{-1}, respectively, when the current densities were reduced back to 200 and 50 mA g^{-1} again, the average discharge capacity of rGO-1 recovery to approximately 182 and 255 mAh g^{-1}, respectively, while the discharge capacities of GO, rGO-6, and rGO-12 are always lower than that of rGO-1 under the same current density. As a result, the rGO-1 cathode material exhibits superior rate capability. More importantly, the rate capability of as-synthesized rGO-1 cathode is higher than the previously reported work[40, 53], which indicated good rate capability. Similar to the results in Fig. 5c, the rGO-0.5 material with the further decrease of reduction degree still show poorer rate capability than the rGO-1 cathode material (see Fig. S6b).

Ex-situ XRD was performed to elucidate the electrochemical reaction process of functionalized rGO with lithium. As shown in Fig. 6a, there was no obvious difference among three XRD patterns of rGO-1 cathodes regardless of the diffraction peaks of aluminum foil, which reveals that no obvious structural change of rGO-1 electrode occurs during charge/discharge processes. Ex-situ XPS further provides some evidences of electrochemical reactions of functionalized rGO with lithium. A strong peak at 55.6 eV in Fig. 6b was detected in the Li 1s region at a discharged state after 3 cycles, while this peak reversibly disappeared upon recharging, suggests lithium ions are reversibly stored upon cycling, and a reversible Li incorporation

occurs via Li–O binding. Further examination of O 1s spectrum of rGO-1 cathode at discharged (Fig. 6c) and charged (Fig. 6d) states revealed that the binding nature of oxygen and carbon reversibly changed upon Li-ion insertion/extraction. Specifically, the quantity of C=O from carboxyl groups decreased and the quantity of C–O increased significantly during discharge, while they oppositely changed once recharging. This important information suggests that the Li ions were electrochemically bound to carboxyl functional groups by breaking the double bonds and forming single bonds between carbon and oxygen. It is worth noting that small change of carbonyl groups in Fig. 6c and 6d indicates that the C=O of carbonyl groups is less active with lithium ions than that of carboxyl functional groups.

The superior cycle performance and rate capability of rGO-1 could be attributed to the considerable oxygen-containing groups, which act as reaction center with lithium ions, and porous microstructure of cross-linked graphene nanosheets, which may lead to fast Li^+ diffusion under high rate charge/discharge conditions. To further understand why various materials exhibit different electrochemical performance, EIS were carried out to evaluate the lithium storage process. The Nyquist plots of GO, rGO-1, rGO-6 and rGO-12 electrodes at a discharged state (1.5 V vs. Li^+/Li) after 10 cycles are compared in Fig. 7. The obtained Nyquist plots are a collective response of kinetic process of rGO reaction with lithium, which consists of one semicircle in the high/medium frequency range and a straight line in the low frequency range. The Nyquist traces were fitted according to an equivalent circuit in inset of Fig. 7, in which R_s is the resistance of the electrolyte; R_{ct} and CPE_{ct} are the charge-transfer

resistance and double-layer capacitance, respectively; Z_w is the Warburg impedance related to the diffusion of lithium ions into the bulk electrodes[54, 55]. According to the fitting parameters listed in Table1, R_s of all samples is similar. R_{ct} of GO, rGO-1, rGO-6 and rGO-12 is 2460, 1059, 594 and 507Ω, respectively. These results demonstrate that the GO electrode possesses higher charge-transfer resistance, which was mainly due to the abundant oxygen content. With the increase of reduction time, the R_{ct} value of rGO samples gradually trail off, suggesting that the rGO materials exhibit higher electrical conductivity. GO cathode materials exhibit poor lithium storage performance for LIBs was mainly due to the poor electrical conductivity, while even the electrical conductivity was improved on account of further reduction, rGO-6 and rGO-12 showed lower electrochemical performance when compared with rGO-1, we can conclude that rGO-1 showed superior electrochemical performance due to the rich oxygen-containing groups on the surface and relatively high electrical conductivity.

In this study, we have developed the facile synthesis of reduced graphene oxide cathode materials. The excellent electrochemical performance of rGO is mainly attributed to the reaction between surface oxygen-containing groups and lithium ions as well as the porous microstructure of graphene framework of the reduced graphene oxide nanosheets. The reversible Li-ion insertion/extraction in rGO during charge/discharge processes was illustrated in Scheme 2. During the discharge process, Li ions were mainly chemically bound to carboxyl functional groups by breaking the double bonds and forming single bonds between carbon and oxygen. Then once

charging, Li ions were reversibly extracted, and the C=O of carboxyl groups may return to their original state. These illustrate that the Li ion storage in carboxyl groups is reversible, more importantly, the carboxyl groups function more electrochemical activity with lithium in comparison to other surface groups on rGO. The porous graphene framework with improved conductivity can increase electron transport rate and expedite Li-ions diffusion from electrolyte to electrode. By controlling the content of oxygen-containing functional groups of rGO and the comparison of electrochemical performance of various rGO electrodes, it can be concluded that increasing oxygen-containing groups results in an increase of the discharge capacity and the excellent electrochemical performance of the rGO is attributed to good electrical conductivity for electron transport as well as abundant oxygen-containing groups especially carboxyl groups which act as the Faradaic reactions centers for efficient Li storage.

4. Conclusion

In summary, poriferous reduced graphene oxide nanosheets were prepared via a facile solution hydrothermal self-assembly route combine with freeze-drying technology for exploring their controllable oxygenic functional groups and their application potential as metal-free cathodes for lithium ion batteries. It was interestingly found that the poriferous reduced graphene oxide nanosheets significantly exhibit excellent electrochemical performance in terms of high capacity,

good rate capability and cycling stability. The excellent electrochemical performance was due to the rich oxygen-containing groups on the surface act as electrochemical active centre for reversible and fast Li storage and highly conducting and porous microstructure of graphene framework work as fast Li^+ diffusion channel in charge/discharge process. These results revealed the application potential of reduced graphene oxide nanosheets as high-performance, environmentally friendly and low-cost cathodes for lithium ion batteries.

Acknowledgements

This research was supported by Key Project of Tianjin Municipal Natural Science Foundation of China (14JCZDJC32200 and 13JCZDJC33900), LPMT, CAEP (KF14006), Academic Innovation Funding of Tianjin Normal University (52XC1404), Scientific Research Foundation for Returned Overseas Chinese Scholars of State Education Ministry, Training Plan of Leader Talent of University in Tianjin and the program of Thousand Youth Talents in Tianjin of China.

Notes and references

1. A. L. Mohana Reddy, S. R. Gowda, M. M. Shaijumon and P. M. Ajayan, *Adv. Mater.*, 2012, **24**, 5045-5064.
2. M. Hu, X. Pang and Z. Zhou, *J. Power Sources*, 2013, **237**, 229-242.
3. Z. S. Wu, A. Winter, L. Chen, Y. Sun, A. Turchanin, X. Feng and K. Mullen,

Adv. Mater., 2012, **24**, 5130-5135.

4. X. Wang, T. Wang, C. Yang, H. Li and P. Liu, *Appl. Surf. Sci.*, 2013, **287**, 242-251.
5. Q. Liu, T. Ohki, D. Liu, H. Sugawara, R. Ishikawa, K. Ueno and H. Shirai, *Nano Energy*, 2015, **11**, 260-266.
6. J. B. Goodenough and Y. Kim, *Chem. Mater.*, 2010, **22**, 587-603.
7. M. S. Whittingham, Y. N. Song, S. Lutta, P. Y. Zavalij and N. A. Chernova, *J. Mater. Chem.*, 2005, **15**, 3362-3379.
8. Y. Shi, S.-L. Chou, J.-Z. Wang, D. Wexler, H.-J. Li, H.-K. Liu and Y. Wu, *J. Mater. Chem.*, 2012, **22**, 16465-16470.
9. B. Cheng, X.-D. Zhang, X.-H. Ma, J.-W. Wen, Y. Yu and C.-H. Chen, *J. Power Sources*, 2014, **265**, 104-109.
10. J. Yang, J. Wang, D. Wang, X. Li, D. Geng, G. Liang, M. Gauthier, R. Li and X. Sun, *J. Power Sources*, 2012, **208**, 340-344.
11. C. Yu, G. Li, X. Guan, J. Zheng, L. Li and T. Chen, *Electrochim. Acta*, 2012, **81**, 283-291.
12. A. Kraytsberg and Y. Ein-Eli, *Adv. Energy Mater.*, 2012, **2**, 922-939.
13. D. Luo, G. Li, C. Fu, J. Zheng, J. Fan, Q. Li and L. Li, *Adv. Energy Mater.*, 2014, **4**, n/a-n/a.
14. S.-K. Jung, H. Gwon, J. Hong, K.-Y. Park, D.-H. Seo, H. Kim, J. Hyun, W. Yang and K. Kang, *Adv. Energy Mater.*, 2014, **4**, n/a-n/a.
15. S. Yang, X. Feng, S. Ivanovici and K. Mullen, *Angew. Chem. Int. Ed.*, 2010,

49, 8408-8411.

16. C. Wang, D. Li, C. O. Too and G. G. Wallace, *Chem. Mater.*, 2009, **21**, 2604-2606.

17. X. Huang, Z. Yin, S. Wu, X. Qi, Q. He, Q. Zhang, Q. Yan, F. Boey and H. Zhang, *Small*, 2011, **7**, 1876-1902.

18. H. Buqa, D. Goers, M. Holzapfel, M. E. Spahr and P. Novák, *J. Electrochem. Soc.*, 2005, **152**, A474.

19. X. Li, Y. Hu, J. Liu, A. Lushington, R. Li and X. Sun, *Nanoscale*, 2013, **5**, 12607-12615.

20. M. Shahid, N. Yesibolati, M. C. Reuter, F. M. Ross and H. N. Alshareef, *J. Power Sources*, 2014, **263**, 239-245.

21. X. Li, X. Meng, J. Liu, D. Geng, Y. Zhang, M. N. Banis, Y. Li, J. Yang, R. Li, X. Sun, M. Cai and M. W. Verbrugge, *Adv. Funct. Mater.*, 2012, **22**, 1647-1654.

22. G. Ji, B. Ding, Z. Sha, J. Wu, Y. Ma and J. Y. Lee, *Nanoscale*, 2013, **5**, 5965-5972.

23. X.-Y. Fan, X.-Y. Shi, J. Wang, Y.-X. Shi, J.-J. Wang, L. Xu, L. Gou and D.-L. Li, *J. Solid State Electrochem.*, 2013, **17**, 201-208.

24. Q. Fan, L. Lei, X. Xu, G. Yin and Y. Sun, *J. Power Sources*, 2014, **257**, 65-69.

25. K. Xu, L.-F. Shen, C.-H. Mi and X.-G. Zhang, *Acta phys. Chim.Sinica*, 2012, **28**, 105-110.

26. H. R. Byon, B. M. Gallant, S. W. Lee and Y. Shao-Horn, *Adv. Funct. Mater.*,

2013, **23**, 1037-1045.

27. B. Z. Jang, C. Liu, D. Neff, Z. Yu, M. C. Wang, W. Xiong and A. Zhamu, *Nano Lett.*, 2011, **11**, 3785-3791.

28. X. Han, C. Chang, L. Yuan, T. Sun and J. Sun, *Adv. Mater.*, 2007, **19**, 1616-1621.

29. A. L. Reddy, S. Nagarajan, P. Chumyim, S. R. Gowda, P. Pradhan, S. R. Jadhav, M. Dubey, G. John and P. M. Ajayan, *Sci. Rep.*, 2012, **2**, 960.

30. H. Kim, H. D. Lim, S. W. Kim, J. Hong, D. H. Seo, D. C. Kim, S. Jeon, S. Park and K. Kang, *Sci. Rep.*, 2013, **3**, 1506.

31. Y. Bai, R. B. Rakhi, W. Chen and H. N. Alshareef, *J. Power Sources*, 2013, **233**, 313-319.

32. L. Jiang and Z. Fan, *Nanoscale*, 2014, **6**, 1922-1945.

33. D. Cai, S. Wang, L. Ding, P. Lian, S. Zhang, F. Peng and H. Wang, *J. Power Sources*, 2014, **254**, 198-203.

34. H. K. Jeong, M. H. Jin, K. P. So, S. C. Lim and Y. H. Lee, *J. Phys. D: Appl. Phys.*, 2009, **42**, 065418.

35. J. Wang, H. S. Wang, K. Wang, F. B. Wang and X. H. Xia, *Sci. Rep.*, 2014, **4**, 6723.

36. H. Qiu, T. Bechtold, L. Le and W. Y. Lee, *Powder Technol.*, 2015, **270**, 192-196.

37. F. Tu, S. Liu, T. Wu, G. Jin and C. Pan, *Powder Technol.*, 2014, **253**, 580-583.

38. D. Lee and J. Seo, *Sci. Rep.*, 2014, **4**, 7419.

39. Y. R. Chen, K. F. Chiu, H. C. Lin, C. Y. Hsieh, C. B. Tsai and B. T. T. Chu, *Mater. Sci. Eng., B*, 2014, **190**, 59-65.

40. W. Ai, Z. Du, Z. Fan, J. Jiang, Y. Wang, H. Zhang, L. Xie, W. Huang and T. Yu, *Carbon*, 2014, **76**, 148-154.

41. D.-W. Wang, C. Sun, G. Zhou, F. Li, L. Wen, B. C. Donose, G. Q. Lu, H.-M. Cheng and I. R. Gentle, *J. Mater. Chem. A*, 2013, **1**, 3607.

42. Y. Liu, R. Deng, Z. Wang and H. Liu, *J. Mater. Chem.*, 2012, **22**, 13619.

43. K. Krishnamoorthy, M. Veerapandian, K. Yun and S. J. Kim, *Carbon*, 2013, **53**, 38-49.

44. S. Pei, J. Zhao, J. Du, W. Ren and H.-M. Cheng, *Carbon*, 2010, **48**, 4466-4474.

45. K. Kakaei and k. hasanpour, *J. Mater. Chem. A*, 2014, DOI: 10.1039/C4TA03026E.

46. C. Botas, P. Álvarez, C. Blanco, R. Santamaría, M. Granda, M. D. Gutiérrez, F. Rodríguez-Reinoso and R. Menéndez, *Carbon*, 2013, **52**, 476-485.

47. A. C. Ferrari, J. C. Meyer, V. Scardaci, C. Casiraghi, M. Lazzeri, F. Mauri, S. Piscanec, D. Jiang, K. S. Novoselov, S. Roth and A. K. Geim, *Phys. Rev. Lett.*, 2006, **97**.

48. J. Hu, Z. Kang, F. Li and X. Huang, *Carbon*, 2014, **67**, 221-229.

49. H.-M. Ju, S. H. Huh, S.-H. Choi and H.-L. Lee, *Mater. Lett.*, 2010, **64**, 357-360.

50. C. Sun, Y. Feng, Y. Li, C. Qin, Q. Zhang and W. Feng, *Nanoscale*, 2014, **6**,

2634-2641.

51. H. Kim, K. Y. Park, J. Hong and K. Kang, *Sci. Rep.*, 2014, **4**, 5278.

52. Z. Du, W. Ai, L. Xie and W. Huang, *J. Mater. Chem. A*, 2014, **2**, 9164-9168.

53. S. H. Ha, Y. S. Jeong and Y. J. Lee, *ACS Appl. Mater. Interfaces*, 2013, **5**, 12295-12303.

54. C. Wang, Z. Guo, W. Shen, Q. Xu, H. Liu and Y. Wang, *Adv. Funct. Mater.*, 2014, **24**, 5511-5521.

55. D. Chao, C. Zhu, X. Xia, J. Liu, X. Zhang, J. Wang, P. Liang, J. Lin, H. Zhang, Z. X. Shen and H. J. Fan, *Nano Lett.*, 2015, **15**, 565-573.

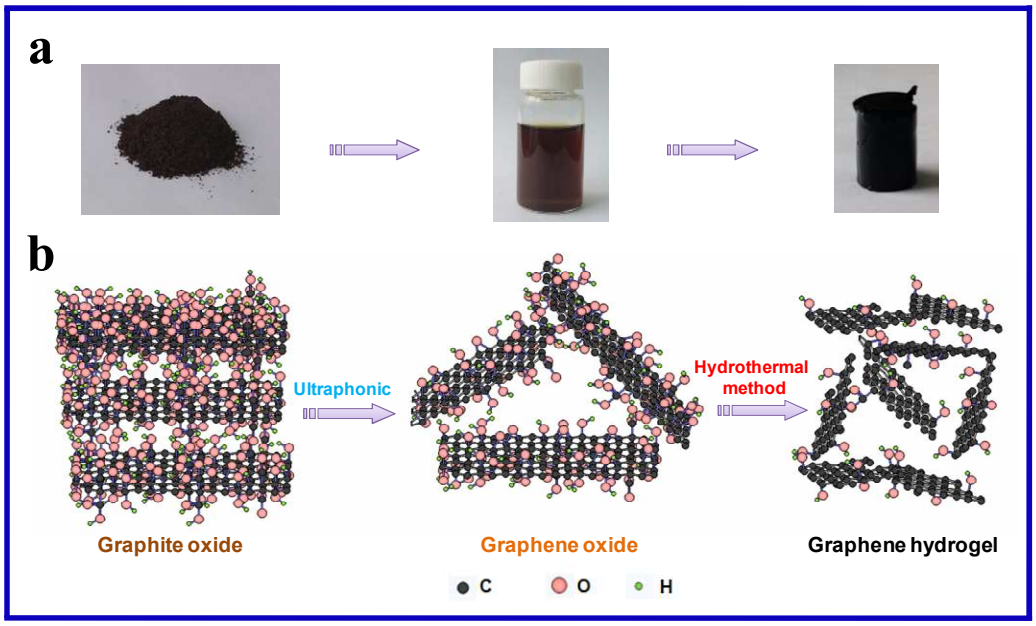

Scheme 1. Schematic illustration of the synthesis process of reduced graphene oxide (rGO).

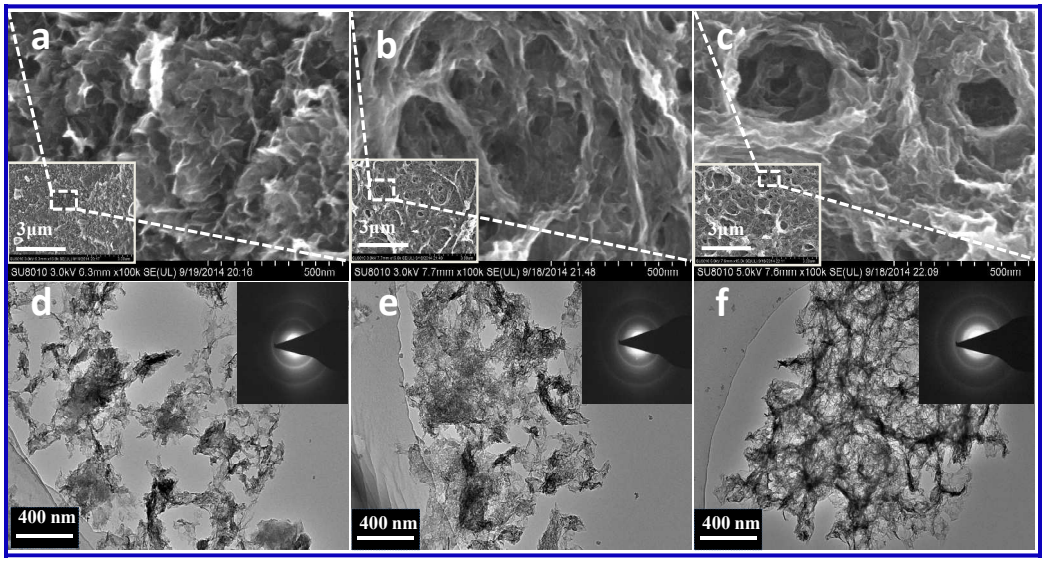

Fig. 1. Typical SEM and TEM images of rGO-1 (a, d), rGO-6 (b, e) and rGO-12 (c, f).

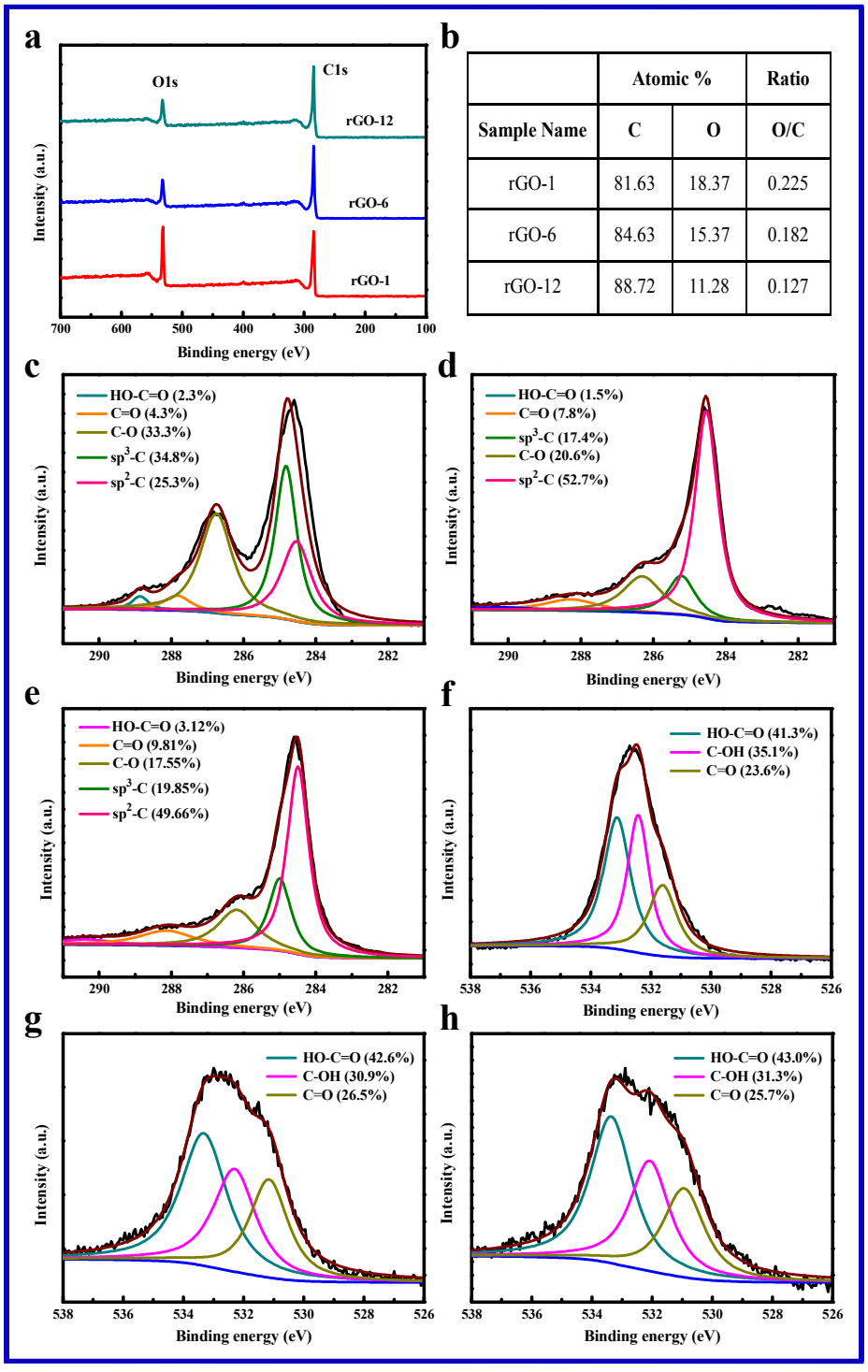

Sample Name	Atomic %		Ratio
	C	O	O/C
rGO-1	81.63	18.37	0.225
rGO-6	84.63	15.37	0.182
rGO-12	88.72	11.28	0.127

Fig. 2. (a) Survey scans of rGO-1, rGO-6 and rGO-12; (b) Summary of atomic ratios O/C on basis of the intensities of C1s and O1s peaks of rGO-1, rGO-6 and rGO-12; The C1s XPS spectra of (c) rGO-1, (d) rGO-6, and (e) rGO-12; The O1s XPS spectra

of (f) rGO-1, (g) rGO-6, and (h) rGO-12.

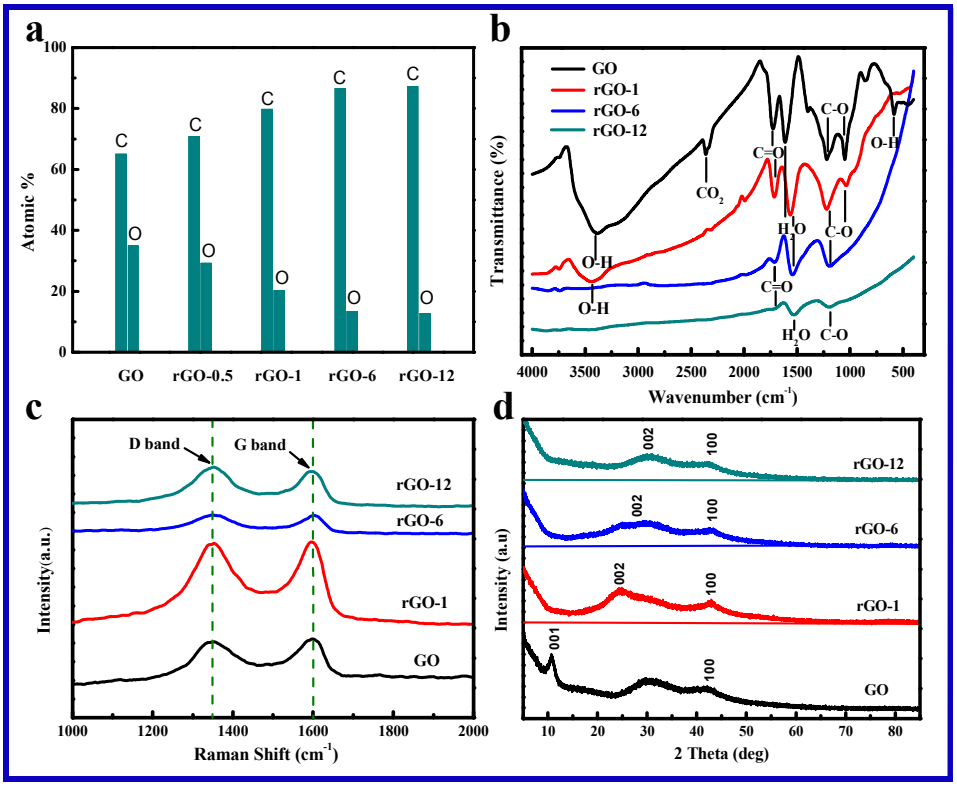

Fig. 3. (a) Elemental distribution data of GO, rGO-0.5, rGO-1, rGO-6 and rGO-12 obtained from EDX; (b) FT-IR spectra of GO, rGO-1, rGO-6 and rGO-12; (c) Raman spectra of GO, rGO-1, rGO-6 and rGO-12; (d) XRD patterns of GO, rGO-1, rGO-6 and rGO-12.

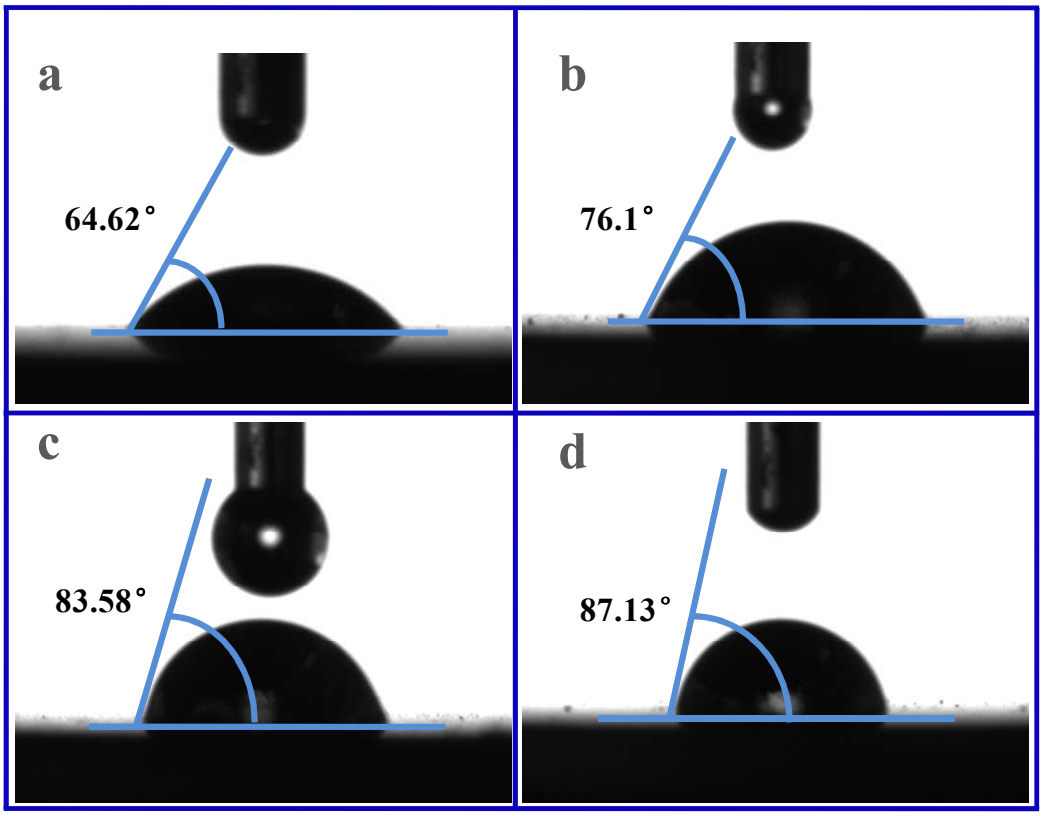

Fig. 4. The hydrophilic angle of the samples: (a) GO, (b) rGO-1, (c) rGO-6 and (d) rGO-12.

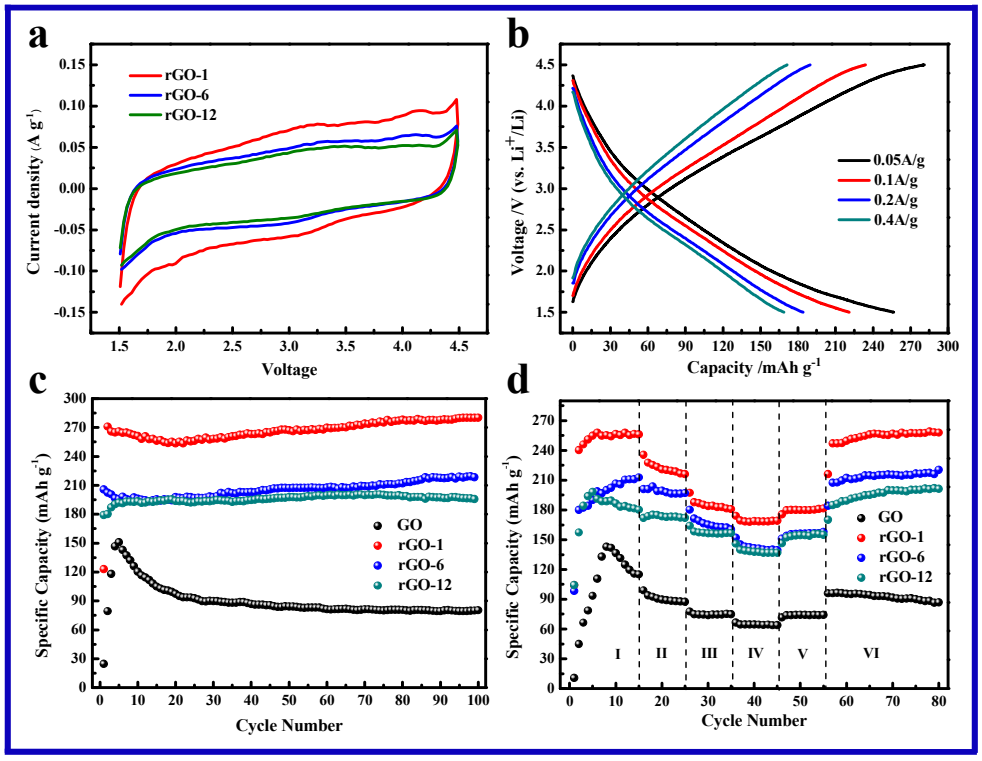

Fig. 5. (a) The CV curves of rGO-1, rGO-6 and rGO-12 samples over a voltage range of 1.5 ~ 4.5 V at a scan rate of 0.1 mV s^{-1}; (b) The charge/discharge profiles of rGO-1 electrode at various current densities; (c) Cycling performance of GO, rGO-1, rGO-6 and rGO-12 electrodes at a current density of 50 mA g^{-1}; (d) Rate performance of GO, rGO-1, rGO-6 and rGO-12 electrodes at various current densities: (I)50, (II)100, (III)200, (IV)400, (V)200, (VI)50 mA g^{-1}.

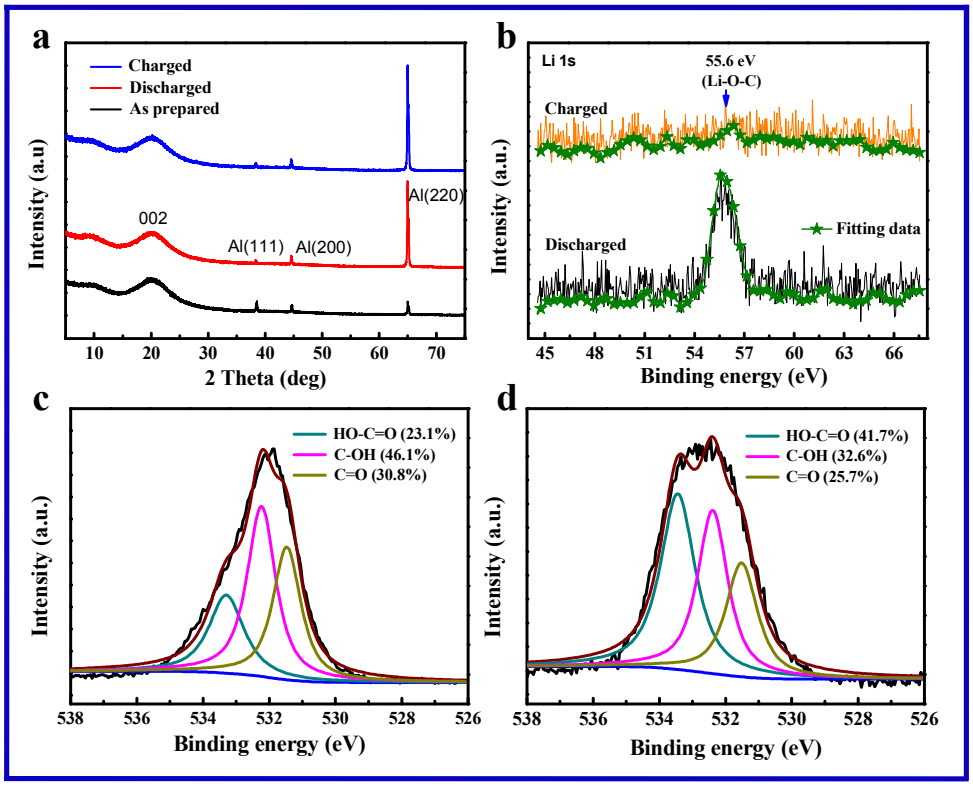

Fig. 6. (a) Ex-situ XRD patterns of rGO-1 cathodes before battery cycling and after 3 cycles at discharged state and charged state, respectively; (b) Ex-situ XPS spectra in Li1s region of rGO-1 cathode after 3 cycles; The ex-site O1s XPS spectra of rGO-1 cathode after 3 cycles at discharged state (c) and charged state (d).

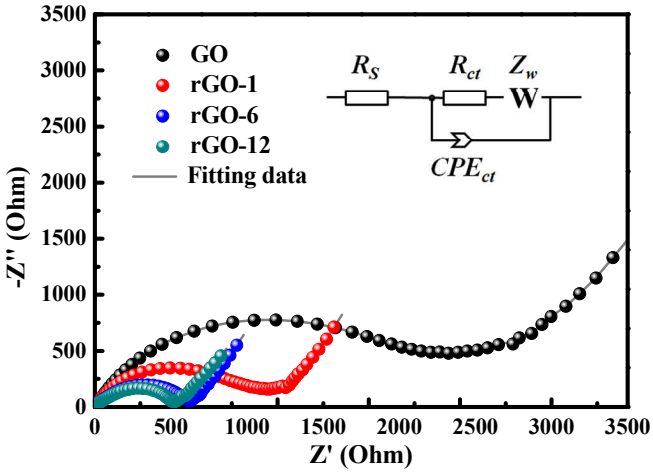

Fig. 7. AC impedance plots and the equivalent circuit for GO, rGO-1, rGO-6 and rGO-12 electrodes at full-discharge state (1.5 V) after 10 cycles.

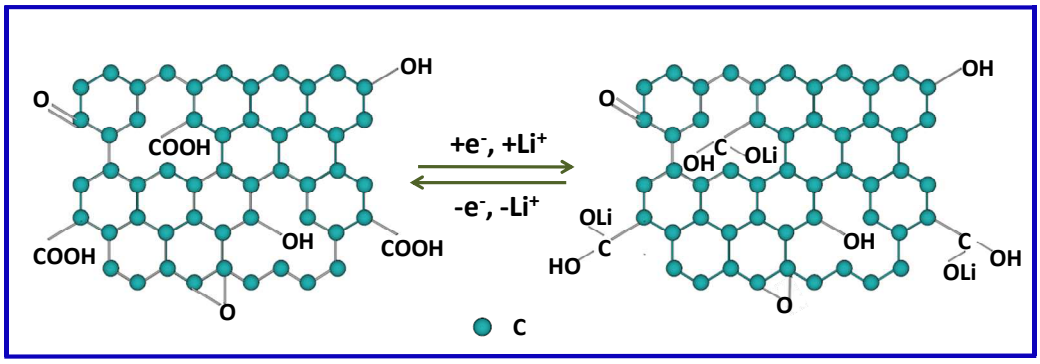

Scheme 2. Schematic diagram for the proposed reversible Li-ion insertion/extraction in the rGO cathode materials.

Table 1 The typical fitted parameters in the electrochemical impedance spectroscopy.

Samples	R_s	R_{ct}	CPE_{ct}	Z_w
GO	4.13	2460	2.88E-05	6349
rGO-1	4.04	1059	2.51E-05	2193
rGO-6	3.47	594	3.64E-05	1342
rGO-12	5.76	507	3.29E-05	2042

Controllable Oxygenic Functional Groups of Metal-free Cathodes for High Performance Lithium Ion Batteries